Very low field F-19 MRI of perfluoro-octylbromide: minimizing chemical shift effects and signal loss due to scalar coupling

Parsa, J.; O'Reilly, T.; Webb, A.

Journal of Magnetic Resonance 325 (2021) 106946

Contents lists available at ScienceDirect

Journal of Magnetic Resonance

journal homepage: www.elsevier.com/locate/jmr

Communication

Very low field ^{19}F MRI of perfluoro-octylbromide: Minimizing chemical shift effects and signal loss due to scalar coupling

Javad Parsa, Thomas O'Reilly, Andrew Webb *

C.J. Gorter Center for High-Field MRI, Leiden University Medical Center, Department of Radiology, Albinusdreef 22333 ZA Leiden, the Netherlands

ARTICLE INFO

Article history:
Received 18 January 2021
Revised 14 February 2021
Accepted 15 February 2021
Available online 20 February 2021

Keywords:
Low field
Fluorine MRI
Turbo-spin echo
Scalar coupling

ABSTRACT

^{19}F images have been obtained from perflurooctylbromide (PFOB) at very low magnetic field (50 mT). The small spectral dispersion (in Hz) means that all fluorine nuclei contribute to the signal without chemical shift artifacts or the need for specialized imaging sequences. Turbo spin echo trains with short interpulse intervals and full 180° refocussing pulses suppress scalar coupling, leading to long apparent T_2 values and highly efficient data collection. Overall, the detection efficiency of PFOB is very similar that of water in tissue.

1. Introduction

After ^{1}H, ^{19}F is the nucleus with the highest gyromagnetic ratio, approximately 91% that of ^{1}H. In biological applications there is essentially zero background signal, which provides high contrast when detecting ^{19}F molecules which have been introduced into the body. A large number of different applications of in vivo ^{19}F magnetic resonance have been shown [1]. For example, various fluorinated gases including sulphur hexafluoride [2], perfluoroethane [3], perfluoropropane [4–5] and most recently octafluorocyclobutane [6–7] have been used for lung imaging. The concentrations of different fluorinated pharmaceuticals including inhalation anesthetics such as halothane [8] and isoflurane, and anti-depressants such as fluoxetine in brain tissue, can also be measured, although the low concentrations mean that MR spectroscopy rather than imaging is used. Another commonly-used class of compounds are liquid perfluorocarbons which have been used in emulsions, nanoparticles and microspheres [9–12]. These can be injected systemically into the bloodstream, and concentrate in the liver and spleen due to macrophage capture with the specific temporal dynamics determined by the physicochemical properties of the particles, and any chemical surface formulations [13]. Alternatively, they can be injected locally to study, for example, oxygenation in the eye [14–15] or tumours [16], since ^{19}F relaxation times are oxygen-dependent [17–19], or report local temperature [20] or pH [21]. Additionally, perfluorocarbon nanoemulsions can quite easily be incorporated in vitro into, for example, mesenchymal cells or non-phagocytic neural stem cells [22–23]. A number of different perfluorocarbons have been used including perfluoro-15-crown-5-ether (PCE) [24], perfluoropolyether (PFP), and perfluoro-octylbromide (PFOB). The former two compounds have the advantage of having either only a single resonance in the case of PCE, or the majority of the fluorine molecules having a single resonance for PFP. Nevertheless, PFOB which contains multiple resonances, is the most commonly-studied compound due to its high level of biocompatibility, having been used as an oxygen carrier and blood volume expander [25]. Multiple studies using targeted PFOB nanoparticles have been published [26].

The major challenges in imaging PFOB are that it contains resonances over a wide chemical shift range (~62 ppm between the $CF_2Br(\alpha)$ and the $CF_2(\gamma)$ resonances), as well as long T_1 and short "effective" T_2 relaxation times: these short effective T_2 values are primarily due to homonuclear F-F scalar coupling[27]. Taken together, these factors mean that specialized pulse sequences must be used: different imaging sequences for ^{19}F imaging have been summarized in an extensive review [28]. For example, one way to address the multiple chemical shifts is to use selective excitation of only one of these peaks, but this approach clearly results in lower signal-to-noise ratio (SNR) than if all the peaks contribute to the image. Selective refocussing pulses can also be used at higher fields to refocus the ^{19}F-^{19}F scalar couplings [27]. The iterative decomposition with echo asymmetry and least-squares estimation (IDEAL) technique has also been used, but requires complex correction for B_0 inhomogeneities [29]. In terms of "overcoming scalar coupling" one approach is to acquire the signal

* Corresponding author.
E-mail address: a.webb@lumc.nl (A. Webb).

https://doi.org/10.1016/j.jmr.2021.106946
1090-7807/

before the spins de-phase, for example by using ultra-short echo time (UTE) [30] or zero echo time (ZTE) [31] imaging, both of which require well-calibrated and fast-switching hardware. UTE can also be combined with steady state free precession (SSFP) for improved sensitivity, but this requires a very homogeneous B_0 field for the gradient echo SSFP sequence. Ghuman et al. [32] compared fast imaging with steady precession (FISP) with turbo spin echo (TSE) sequences, concluding that FISP is better for a low number of slices, whereas TSE is advantageous for a larger number of slices.

Although most fluorine studies are performed on either high field preclinical systems, or research-oriented clinical human systems, the hardware and software interfaces required are not standard, and the number of systems capable of performing even simple experiments is quite limited. In this work we set out to see if ^{19}F imaging of PFOB could potentially be performed on a very simple and inexpensive low field MRI system, operating at 50 mT [33]. The obvious disadvantage of low field is the lower intrinsic SNR. However, there are also a number of potential advantageous features which at least partially mitigate the low sensitivity. First, the spectral dispersion of PFOB in Hz is very small (~125 Hz), which is less than the typical imaging pixel bandwidth and the homogeneity of the magnet, and so all resonances can be imaged with no chemical shift artifacts without recourse to specialized sequences. Second, the T_1 relaxation time is significantly shorter due to the frequency dependence of the dipole–dipole coupling mechanism. Third, the effective T_2 values can be very long if the dephasing effects of homonuclear scalar coupling and the fast T_2 relaxation of anti-phase coherence [34] can be largely removed by using very short echo times. With this approach very long echo train length (ETL) TSE sequences with full 180° refocussing pulses can be used for efficient data acquisition due to the much lower specific absorption rate (SAR) at low field. Indeed the T_2/T_1 ratio, a figure-of-merit in terms of the relaxation-time determined sensitivity, can approach unity for PFOB, which is one to two orders of magnitude greater than typically found for conventional high field readouts.

2. Methods

2.1. Low-field MRI system

The system operating at 50 mT (2.15 MHz ^1H, 2.02 MHz ^{19}F) has been described in detail previously [33] and consists of a Halbach magnet of twenty three rings, with two layers of N48 neodymium boron iron (NdBFe) magnets ($12 \times 12 \times 12$ mm^3) per ring. The array has a clear bore of 27 cm, and a length of 50 cm between the two outer rings. An additional shim ring filled using $3 \times 3 \times 3$ mm N45 NdBFe magnets was used to improve the B_0 field homogeneity. The total weight of the magnet including all components is ~ 75 kg. The magnet is positioned inside a $62.5 \times 62.5 \times 85$ cm Faraday cage constructed from 2 mm thick aluminium sheets. Gradients coils consist of 1.5 mm diameter copper wire pressed and glued into 3D printed formers. The efficiencies of the x, y and z gradient coils are 0.59, 0.95 and 1.02 mT/m/A, respectively. A triple-axis custom-designed gradient amplifier produces an output gain of 3.3 Amps per 1 V input from the +/- 10 V 16-bit digital-to-analogue (DAC) gradient drivers of the MR console (Magritek Kea 2, Aachen, Germany). The RF pulses generated by the spectrometer are amplified by a custom built 1 kW RF amplifier.

2.2. Switchable MR coil

There are a whole slew of designs for double-tuned $^1H/^{19}F$ RF coils in the literature, see for example Villa-Valverde and references therein [35]. However, due to the very close frequencies between ^1H (2.15 MHz) and ^{19}F (2.02 MHz) at 50 mT, the most simple approach is to have a switchable unit, which can either consist of a mechanical switch (shown here) or one which can be electronically switched using a TTL-controlled relay. The solenoid coil was fabricated on a plexiglass cylinder by using copper tape of 5 mm width and 0.07 mm thickness. Dimensions are 15 cm length and 9 cm outer diameter/8.5 cm inner diameter with 15 turns. Impedance matching used a conventional L-network. The parallel "tuning capacitor" had a value of 513 pF (ATC Type E, non-magnetic) for ^1H and 590 pF for ^{19}F. To switch tuning of the coil from ^1H to ^{19}F a mechanical switch was used which connected the extra 77 pF of capacitance. Because the resonance frequencies of ^1H and ^{19}F are so close to each other there is a negligible difference between the required value of the matching capacitor, in this case 140 pF.

3. Data acquisition

3.1. Phantom preparation

Pure PFOB was obtained from Sigma-Aldrich, Netherlands. A plastic cylinder length 4 cm, inner diameter 8 mm, volume 2 mL, was filled with PFOB. An identical cylinder was filled with water doped with copper sulphate to give a T_2 value of 150 ms, which is slightly higher than the field-independent value proposed in [36]: we deliberately chose a slightly conservative value for the SNR comparison between ^1H and ^{19}F presented at the end of this paper. A third cylinder was filled with fomblin, a long-chain perfluorocarbon with chemical shift range from −52 to −94 ppm (-104 to −188 Hz).

3.2. Relaxation time measurements

T_1 relaxation times were measured using a spectroscopic inversion-recovery sequence: a standard four-element phase cycle was used. The data were fitted with a three-parameter (S_0, T_1, and inversion-efficiency) curve to account for any B_1-inhomogeneities [37]. Experiments were repeated six times and the standard deviation of the measurements calculated. T_2 values were measured using a spectroscopic Carr-Purcell-Meiboom-Gill (CPMG) sequence with an eight-step phase cycle. The interpulse time was varied, with a minimum of ~ 2.5 ms set by the length of the 90 and 180° RF pulses (100 μs at a power of 4 and 16 Watts, respectively) and various times required for blanking, receiver turn-on, and post-acquisition delays. Experiments were repeated six times and the standard deviation of the measurements calculated.

3.3. Imaging

Images were acquired from a phantom containing one tube of PFOB and one of fomblin (dimensions as described previously) using a custom-programmed 3-dimensional TSE sequence, with the phase encoding gradient unwound between successive acquisitions. For all images presented the field-of-view was $80 \times 80 \times 60$ mm, with a data matrix of $64 \times 64 \times 8$, and an acquisition bandwidth of 30 kHz. The minimum interpulse delay, with gradient switching in addition to the considerations mentioned above, was 5 ms. Different k-space trajectories (in-out, linear and out-in) were acquired, as reported in the specific figure legends. For all images, an ETL of 64 was used, a TR of 4 s (to remove any T_1-weighting) was used between each of the eight phase-encoding steps in the third dimension: no signal averaging was used. Data were exported and processed using a custom-written Python script. A multi-dimensional Gaussian filter (scipy.ndimage.gaussian_filter, sigma = 2) is applied to the raw k-space data prior

to Fourier transformation. In each figure the central image from the 3D data set is shown. 90° and 180° pulses were all 100 μs duration, with appropriate calibrated pulse powers of 4 and 16 Watts, respectively, for both ^{1}H and ^{19}F.

For the comparison between proton and fluorine SNRs, a spin-echo sequence was run with TR = 10 s and TE = 5 ms to minimize T_1 and T_2 effects. Two signal averages were acquired, no filtering was applied.

4. Results

Fig. 1 shows a photograph of the RF coil, together with network analyzer plots of the responses with the switch in each position. The quality (Q) factor values of the coil are 90 (2.02 MHz) and 87 (2.15 MHz), giving coil bandwidths on the order of 20 kHz. The Q-values for the situation in which the switch was removed are essentially identical. A frequency shift of less than 1 kHz is introduced by the switch.

For the PFOB sample the T_1 was measured to be 720 ± 10 ms. Fig. 2 shows CPMG data for four interpulse delays (τ) for PFOB, fomblin and doped water: the total echo train duration was kept constant at 150 ms. The results show a significant reduction in T_2 value as a function of τ for PFOB, a smaller dependence for fomblin, and a value which does not vary for water.

Fig. 3(a) shows the variation in measured T_2 values as a function of interecho timing between 2.5 and 10 ms for PFOB . There is a drop of almost one order-of-magnitude over this range. The standard deviation of these measurements is less than 3% of the absolute value. Using these values one can calculate the relative signal of each echo of a TSE imaging sequence for different echo times, as shown in Fig. 3(b):

$$SNR_N \propto exp\frac{-N\tau}{T_{2.eff}(\tau)}$$

where N is the echo number, and the term $T_{2,eff}(\tau)$ emphasizes the fact that the effective transverse relaxation rate is a function of τ. Fig. 3(c) shows the corresponding point spread functions (PSFs), calculated via the Fourier transform of these exponential decay functions. The PSF is a measure of the spatial resolution of the image, comprising the digital resolution (field-of-view divided by the number of acquired data points) convolved with the broadening due to the Fourier transform of the decaying exponential function: a broader PSF indicates a more blurred image.

In a TSE sequence the effective echo time (TE_{eff}) is usually defined as the value at which the k_{phase} = 0 line in k-space is acquired. By altering the order in which k-space is covered this value can correspond to any echo number shown in Fig. 3(b). Here, we consider three commonly-used cases: an "in-out trajectory" in which the k_{phase} = 0 line is sampled first, a "linear trajectory" in which k_{phase} = 0 sampled half way through the echo train, and an "out-in trajectory" in which k_{phase} = 0 corresponds to the final echo of the train. The SNR is clearly highest for the in-out trajectory: the major mitigating factor is that blurring artifacts can be quite apparent if the echo train length is on the order of the effective T_2.

To illustrate the effect of TE_{eff} on image quality, Fig. 4 shows images acquired with an in-out trajectory from a phantom with one tube of PFOB and one tube of fomblin. Fomblin has an effective T_2 value of ~ 95 ms at a τ value of 5 ms, which is only slightly reduced as a function of τ. Two effects in Fig. 4 are apparent: the substantial decrease in SNR for even very small differences in the value of τ, and the increase in the point spread function (PSF) in the phase encoding direction for higher τ values, with the latter effect being much greater for the shorter T_2 value of fomblin.

Fig. 5 shows results using the linear and out-in k-space trajectories. As expected the absolute SNR is lower than for the in-out trajectory (in-out ~ 80:1, linear ~ 50:1, out-in ~ 22:1 for PFOB), but the difference in signal intensity between PFOB and fomblin is much larger, i.e. one can potentially differentiate between different perfluorocarbons based on their τ-dependent relaxation times.

The final experiments were performed to assess the relative SNR of ^{1}H and ^{19}F PFOB images at 50 mT. By considering the respective values for H_2O and PFOB: molecular weights (18 and 498), densities (1 g/mL and 1.92 g/mL), number of protons (two) and fluorine atoms (seventeen) per molecule, and gyromagnetic ratios (42.58 MHz/T and 40.31 MHz/T), the theoretical relative SNRs (ignoring relaxation) for water and PFOB are 1.93:1. Fig. 6 (a) shows an experimental comparison, with the value obtained being 2.02:1, in reasonable agreement with theory. The remainder of Fig. 6 shows images acquired with different k-space trajectories with an inter-echo spacing of 5 ms to maximize SNR. The in-out trajectory results in a similar SNR ratio of 2.17:1, with this ratio decreasing for linear and out-in trajectories, as expected due to the shorter T_2 of water at this inter-echo time.

5. Discussion

The results shown here demonstrate that ^{19}F MRI of multi-resonance homonuclear scalar coupled perfluorocarbons such as PFOB, which are the compounds which have been demonstrated to have a high degree of biocompatibility, may be feasible for certain in vivo applications at low field. Although there is a far lower net magnetization available compared to the higher magnetic

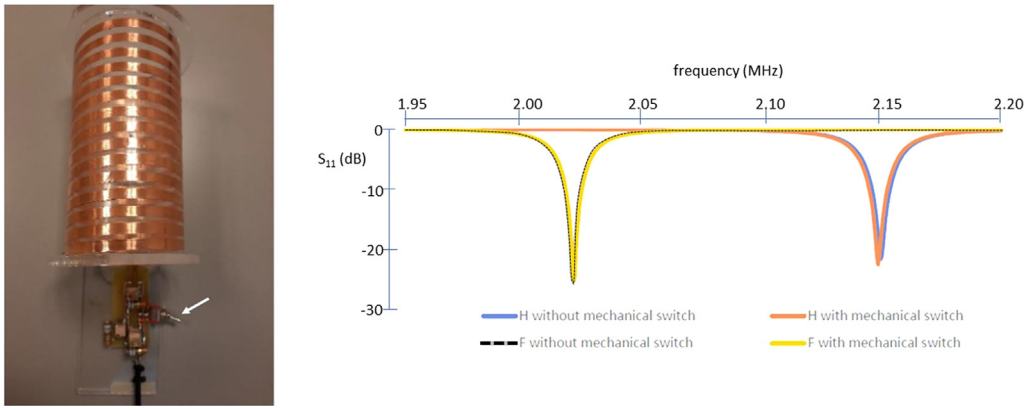

Fig. 1. (left) Photograph of the solenoid coil which can be switched between ^{1}H and ^{19}F using a mechanical switch (arrow). (right) S_{11} plots of the ^{1}H and ^{19}F switched-mode RF coil. A comparison with/without the low-loss mechanical switch shows negligible differences.

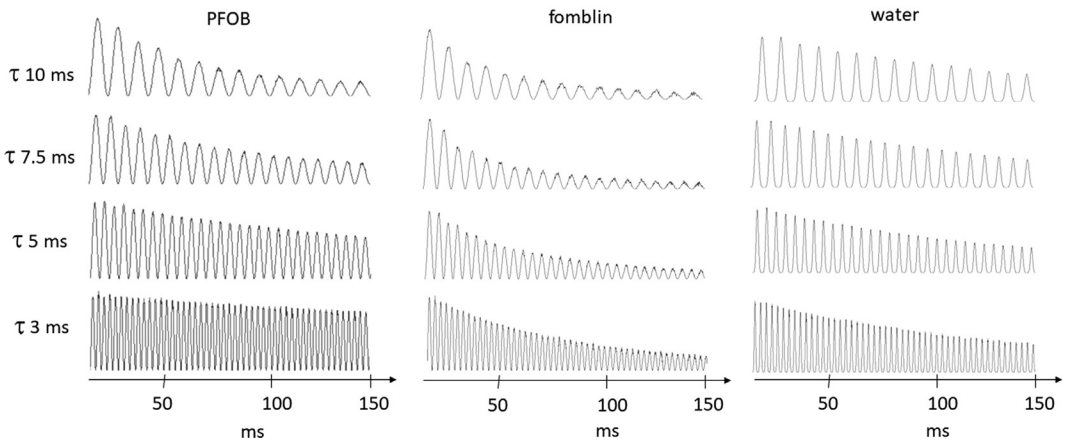

Fig. 2. Four different CPMG echo trains plotted as a function of interpulse time (τ) for PFOB, fomblin and water for a constant overall echo train duration of 150 ms.

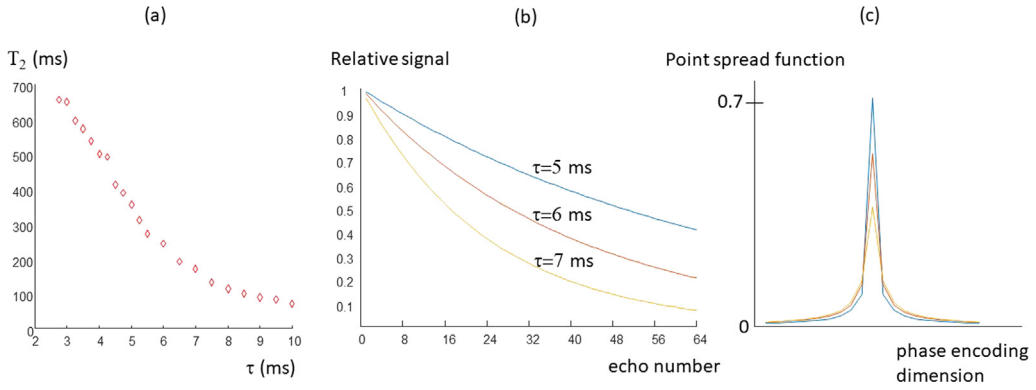

Fig. 3. (a) Measured T_2 value from a CPMG echo train for PFOB as a function of the interpulse delay τ. (b) Corresponding calculated SNR as a function of echo number for a TSE sequence with different inter-echo times. (c) Corresponding point spread function (PSF) for the three values of τ.

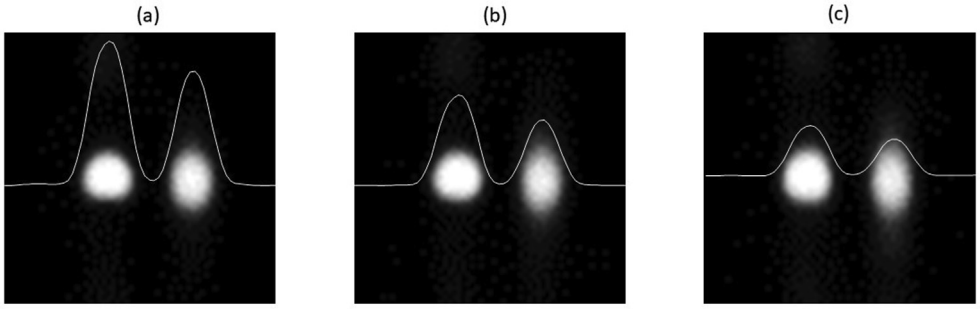

Fig. 4. TSE images acquired from a tube containing PFOB (left) and fomblin (right) with different inter-echo times for an in-out k-space trajectory: (a) τ = 5 ms, (b) τ = 6 ms, (c) τ = 7 ms. The frequency encoding direction left–right and the phase-encoding direction up-down. Projections are shown through the horizontal mid-line of the image.

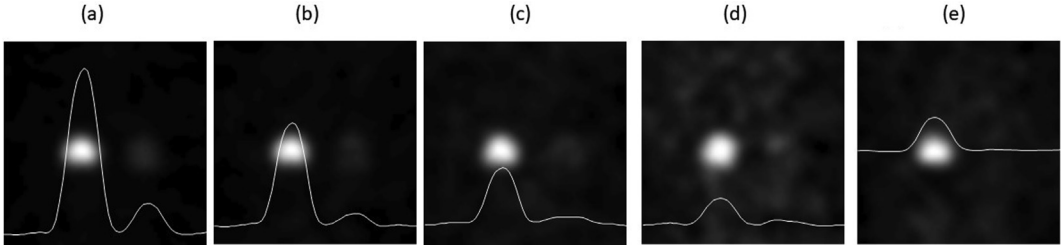

Fig. 5. TSE images acquired from a tube containing PFOB (left) and fomblin (right) with different inter-echo times for linear and out-in k-space trajectories: (a) linear τ = 5 ms, (b) linear τ = 6 ms, (c) linear τ = 7 ms, (d) linear τ = 8 ms, and (e) out-in τ = 5 ms.

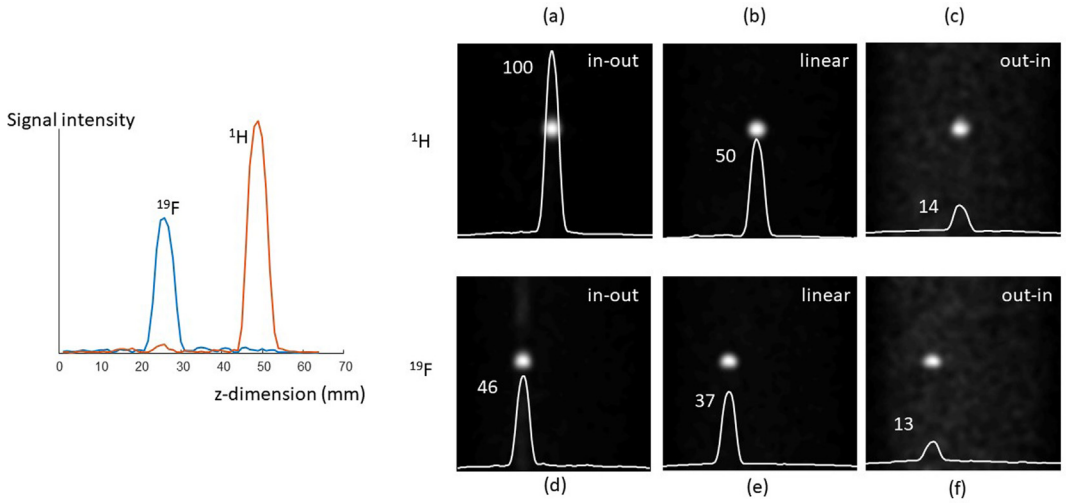

Fig. 6. (left) Superimposed one-dimensional projections of a tube containing PFOB (blue) and one containing doped water (orange) with the coil mechanically switched between ^{1}H and ^{19}F for consecutive acquisitions. The relative SNRs were 2.02:1. (right) Images acquired with different k-space trajectories for ^{1}H (top row) and ^{19}F (bottom row), with SNRs indicated. Imaging parameters as described previously. (For interpretation of the references to colour in this figure legend, the reader is referred to the web version of this article.)

fields typically used for ^{19}F MRI, there are several advantages that can be exploited at low field. First, the absolute chemical shift dispersion (in Hz) at fields of ~ 100 mT or lower is less than the imaging pixel bandwidth and so all of the resonances in the molecule give rise to usable signal without producing image artifacts. Second, the reduced SAR at low fields allows rapid pulsing of high tip angle i.e. 180° refocussing pulses with very short interpulse delays. The use of very short interpulse delays ($\tau \ll J_{F\text{-}F}$) is also very efficient at refocussing scalar coupling evolution, meaning that the transverse magnetization can be recycled using repeated refocusing pulses, allowing much longer ETLs and therefore higher imaging efficiency in TSE sequences. Since the interpulse delay is ~ 40 times longer than the pulse duration (100 μs), there is a very small contribution from spin-locking, meaning that the longer effective transverse relaxation time can be attributed primarily to homonuclear scalar coupling refocusing. Finally, the T_1 time is shorter than at field strengths used for clinical or preclinical studies (e.g. T_1 ~ 1200 ms at 3 T [38], allowing more efficient data acquisition when signal averaging is required for applications which have an intrinsically low sensitivity due to the low concentrations of ^{19}F in tissue.

Of course in vivo imaging typically involves a much lower concentration of ^{19}F molecules compared to tissue water. However, as shown by many authors [39–41], so-called "hot-spot" ^{19}F is sufficient, in which two-dimensional projection images are acquired and overlaid on a 3D proton image. Indeed from the data shown in Fig. 6 it is clear that the intrinsic SNR of ^{19}F of PFOB and ^{1}H of tissue water are very similar. ^{1}H TSE images are typically acquired with a linear k-space trajectory to introduce a degree of T_2-weighting to distinguish between different organs, and the data shown in Fig. 6 show very similar SNRs for a linear k-space trajectory for ^{1}H image, Fig. 6(b), and an in-out trajectory for the ^{19}F image, Fig. 6(d). Of course the T_2 relaxation time of PFOB and other perfluorocarbons might be reduced by emulsification and also by the effects of sequestration in-vivo: these effects definitely need to be investigated in future studies.

In this study we used very high duty cycle TSE sequences due to the very low SAR at low field. Although TSE sequences can be optimized at higher fields [38], other types of sequence have been suggested to achieve the optimal SNR. Ultrashort echo time (UTE) [5] and steady state free precession techniques [4] have been shown to provide the highest SNR. These types of sequences pose significant challenges at low-field using custom-built, inexpensive hardware. UTE sequences require very rapid switching transmit/receive switches and rapid ring-down of the RF coil. Given the relatively high Q-values of the coils in this study, some form of feedback or active damping would have to be enacted [42–43], as well as a custom-design of an actively-driven transmit/receive switch. For SSFP sequences a high degree of B_0 homogeneity is required in order to avoid banding artifacts, and practical Halbach arrays with finite length typically have inhomogeneity values which make these sequences difficult to implement successfully (note though that SSFP sequences have been used on a much larger electromagnetic-based ultra-low-field system [44].

One of the recent innovations in fluorine imaging has been "multicolour" or "multispectral" data acquisition [45], in which the different chemical shifts of separate fluorine compounds can be used to distinguish differential biodistribution. Obviously at very low field this is not possible, but one can potentially use the different degrees of scalar coupling, and the corresponding dependence of the effective T_2 time on the value of τ for distinguishing between compounds. This can be seen in the data shown in Figs. 4 and 5. In Fig. 4, using an in-out trajectory there is relatively little contrast between the signals from PFOB and fomblin, whereas in Fig. 5 using a linear or out-in trajectory the contrast is much higher, albeit at the price of a lower SNR.

Finally, we note that image acquisition efficiency can be increased by interleaving ^{1}H and ^{19}F imaging. This can be performed using electronically switched coils, for example. The longer T_1 of ^{19}F PFOB compared to tissue water means that after a single 2D ^{19}F single-shot readout has been acquired, then a significant part of the 3D ^{1}H k-space could be acquired. Interleaved readout of both ^{1}H and ^{19}F also has the advantage that any motion can be corrected [46]. Similar approaches have been used previously for both ^{19}F [46] as well as other nuclei such as ^{31}P [47], ^{23}Na [48] and ^{13}C [47].

It is important to stress that the approach used here only results in improvements in data acquisition efficiency for perfluorocarbons which contain multiple homonuclear scalar coupled resonances. So applications such as gaseous imaging with mono-resonant compounds such as SF_6, with a very low concentration of ^{19}F nuclei to start with, are far more suited to convential high field approaches. Similarly, many researchers use PCE-filled nanoparticles in for cell-tracking in preclinical studies, and since

PCE contains a single ^{19}F resonance, the SNR loss for low field compared to high field would follow directly from Boltzmann considerations.

6. Conclusion

^{19}F MRI of perfluorocarbons with multiple resonances (~62 ppm range) does not suffer from chemical shift induced image artifacts at 50 mT. The effective T_2 of the resonances becomes longer at very short interpulse times in a CPMG sequence due to suppression of ^{19}F-^{19}F scalar coupling. Using long echo train length TSE sequences, very efficient ^{19}F data acquisition has been demonstrated.

Declaration of Competing Interest

The authors declare that they have no known competing financial interests or personal relationships that could have appeared to influence the work reported in this paper.

Acknowledgement

This work was supported by the NWO Simon Stevin Meester Prize and H2020-MSCA-ITN-ETN 859908.

References

[1] S. Waiczies, M. Srinivas, U. Flogel, P. Boehm-Sturm, T. Niendorf, Special issue on fluorine-19 magnetic resonance: technical solutions, research promises and frontier applications, Magn. Reson. Mater. Phy. 32 (1) (2019) 1–3.
[2] N.L. Adolphi, D.O. Kuethe, Quantitative mapping of ventilation-perfusion ratios in lungs by 19F MR imaging of T1 of inert fluorinated gases, Magn. Reson. Med. 59 (4) (2008) 739–746.
[3] L. Carrero-Gonzalez, T. Kaulisch, D. Stiller, In vivo diffusion-weighted MRI using perfluorinated gases: ADC comparison between healthy and elastase-treated rat lungs, Magn. Reson. Med. 70 (6) (2013) 1761–1764.
[4] A. Maunder, H.F. Chan, P.J.C. Hughes, G. Collier, G. Norquay, O. Rodgers, P. Thelwall, F. Robb, M. Rao, J.M. Wild, MR properties of (19) F C3 F8 gas in the lungs of healthy volunteers: T 2 * and apparent diffusion coefficient at 1.5T and T 2 * at 3T, Magn. Reson. Med., (2020).
[5] M.J. Couch, I.K. Ball, T. Li, M.S. Fox, S.L. Littlefield, B. Biman, M.S. Albert, Pulmonary ultrashort echo time 19F MR imaging with inhaled fluorinated gas mixtures in healthy volunteers: feasibility, Radiology 269 (3) (2013) 903–909.
[6] Pavlova OS, Anisimov NV, Gervits LL, Gulyaev MV, Semenova VN, Pirogov YA, Panchenko VY. (19) F MRI of human lungs at 0.5 Tesla using octafluorocyclobutane. Magn Reson Med 2020;84(4):2117-2123.
[7] Y. Shepelytskyi, T. Li, V. Grynko, C. Newman, F.T. Hane, M.S. Albert, Evaluation of fluorine-19 magnetic resonance imaging of the lungs using octafluorocyclobutane in a rat model, Magn. Reson. Med. (2020).
[8] D.K. Menon, G.G. Lockwood, C.J. Peden, I.J. Cox, J. Sargentoni, J.D. Bell, G.A. Coutts, J.G. Whitwam, In-Vivo F-19 Magnetic-Resonance Spectroscopy of Cerebral Halothane in Postoperative-Patients - Preliminary-Results, Magnet. Reson. Med. 30 (6) (1993) 680–684.
[9] V. Herynek, M. Martiniskova, Y. Bobrova, A. Galisova, J. Kotek, P. Hermann, F. Koucky, D. Jirak, M. Hajek, Low-molecular-weight paramagnetic (19)F contrast agents for fluorine magnetic resonance imaging, Magn. Reson. Mater. Phy. 32 (1) (2019) 115–122.
[10] D. Jirak, A. Galisova, K. Kolouchova, D. Babuka, M. Hruby, Fluorine polymer probes for magnetic resonance imaging: quo vadis?, Magn. Reson. Mater. Phy. 32 (1) (2019) 173–185.
[11] E. Hequet, C. Henoumont, R.N. Muller, S. Laurent, Fluorinated MRI contrast agents and their versatile applications in the biomedical field, Future Med. Chem. 11 (10) (2019) 1157–1175.
[12] A.G. Webb, M. Wong, K.J. Kolbeck, R.L. Magin, K.S. Suslick, Sonochemically produced fluorocarbon microspheres: A new class of magnetic resonance imaging agent, J. Magn. Reson. Imaging 6 (4) (1996) 675–683.
[13] O.S. Pavlova, M.V. Gulyaev, N.V. Anisimov, D.N. Silachev, L.L. Gervits, Y.A. Pirogov, New Aspects of Biodistribution of Perfluorocarbon Emulsions in Rats: Thymus Imaging, Appl. Magn. Reson. (2020).
[14] C.A. Wilson, B.A. Berkowitz, D.L. Hatchell, Oxygen Kinetics in Preretinal Perfluorotributylamine, Exp. Eye Res. 55 (1) (1992) 119–126.
[15] C.A. Wilson, B.A. Berkowitz, B.W. Mccuen, H.C. Charles, Measurement of Preretinal Oxygen-Tension in the Vitrectomized Human Eye Using F-19 Magnetic-Resonance Spectroscopy, Arch. Ophthalmol.-Chic. 110 (8) (1992) 1098–1100.
[16] V. Spanoudaki, J.C. Doloff, W. Huang, S.R. Norcross, S. Farah, R. Langer, D.G. Anderson, Simultaneous spatiotemporal tracking and oxygen sensing of transient implants in vivo using hot-spot MRI and machine learning, P. Natl. Acad. Sci. USA 116 (11) (2019) 4861–4870.
[17] B.J. Dardzinski, C.H. Sotak, Rapid Tissue Oxygen-Tension Mapping Using F-19 Inversion-Recovery Echo-Planar Imaging of Perfluoro-15-Crown-5-Ether, Magnet. Reson. Med. 32 (1) (1994) 88–97.
[18] P.S. Hees, C.H. Sotak, Assessment of Changes in Murine Tumor Oxygenation in Response to Nicotinamide Using F-19 Nmr Relaxometry of a Perfluorocarbon Emulsion, Magnet. Reson. Med. 29 (3) (1993) 303–310.
[19] C.H. Sotak, B.J. Dardzinski, R.J. Kaufman, Tissue Oxygenation Measurements Using F-19 Nmr Imaging of Perfluoro-15-Crown-5-Ether Emulsions, Abstr. Pap. Am. Chem. S 207 (1994), 34-Coll..
[20] B.A. Berkowitz, J.T. Handa, C.A. Wilson, Perfluorocarbon Temperature-Measurements Using F-19 Nmr, Nmr. Biomed. 5 (2) (1992) 65–68.
[21] X.N. Huang, G. Huang, S.R. Zhang, K. Sagiyama, O. Togao, X.P. Ma, Y.G. Wang, Y. Li, T.C. Soesbe, B.D. Sumer, M. Takahashi, A.D. Sherry, J.M. Gao, Multi-Chromatic pH-Activatable F-19-MRI Nanoprobes with Binary ON/OFF pH Transitions and Chemical-Shift Barcodes, Angew. Chem. Int. Ed. 52 (31) (2013) 8074–8078.
[22] S.S. Moonshi, C. Zhang, H. Peng, S. Puttick, S. Rose, N.M. Fisk, K. Bhakoo, B.W. Stringer, G.G. Qiao, P.A. Gurr, A.K. Whittaker, A unique F-19 MRI agent for the tracking of non phagocytic cells in vivo, Nanoscale 10 (17) (2018) 8226–8239.
[23] M. Srinivas, M.S. Turner, J.M. Janjic, P.A. Morel, D.H. Laidlaw, E.T. Ahrens, In Vivo Cytometry of Antigen-Specific T Cells Using F-19 MRI, Magnet. Reson. Med. 62 (3) (2009) 747–753.
[24] C.H. Sotak, P.S. Hees, H.N. Huang, M.H. Hung, C.G. Krespan, S. Raynolds, A New Perfluorocarbon for Use in F-19 Magnetic-Resonance-Imaging and Spectroscopy, Magnet. Reson. Med. 29 (2) (1993) 188–195.
[25] J.G. Riess, Oxygen carriers ("blood substitutes")–raison d'etre, chemistry, and some physiology, Chem. Rev. 101 (9) (2001) 2797–2920.
[26] L. Wu, F. Liu, S. Liu, X. Xu, Z. Liu, X. Sun, Perfluorocarbons-Based (19)F Magnetic Resonance Imaging in Biomedicine, Int. J. Nanomed. 15 (2020) 7377–7395.
[27] C. Giraudeau, J. Flament, B. Marty, F. Boumezbeur, S. Meriaux, C. Robic, M. Port, N. Tsapis, E. Fattal, E. Giacomini, F. Lethimonnier, D. Le Bihan, J. Valette, A new paradigm for high-sensitivity 19F magnetic resonance imaging of perfluorooctylbromide, Magn. Reson. Med. 63 (4) (2010) 1119–1124.
[28] A.H. Schmieder, S.D. Caruthers, J. Keupp, S.A. Wickline, G.M. Lanza, Recent Advances in (19)Fluorine Magnetic Resonance Imaging with Perfluorocarbon Emulsions, Engineering (Beijing) 1 (4) (2015) 475–489.
[29] K.D. Ludwig, D. Hernando, N.T. Roberts, R.B. van Heeswijk, S.B. Fain, A chemical shift encoding (CSE) approach for spectral selection in fluorine-19 MRI, Magnet. Reson. Med. 79 (4) (2018) 2183–2189.
[30] J. Rahmer, P. Bornert, J. Groen, C. Bos, Three-dimensional radial ultrashort echo-time imaging with T2 adapted sampling, Magn. Reson. Med. 55 (5) (2006) 1075–1082.
[31] F. Schmid, C. Holtke, D. Parker, C. Faber, Boosting (19) F MRI-SNR efficient detection of paramagnetic contrast agents using ultrafast sequences, Magn. Reson. Med. 69 (4) (2013) 1056–1062.
[32] H. Ghuman, T.K. Hitchens, M. Modo, A systematic optimization of F-19 MR image acquisition to detect macrophage invasion into an ECM hydrogel implanted in the stroke-damaged brain, Neuroimage 202 (2019).
[33] T. O'Reilly, W.M. Teeuwisse, D. de Gans, K. Koolstra, A.G. Webb, In vivo 3D brain and extremity MRI at 50 mT using a permanent magnet Halbach array, Magn. Reson. Med. 85 (2021) 495–505.
[34] T. Meersmann, G. Bodenhausen, Transverse Relaxation in Proton Nmr - Separate Measurement of Decay-Rates of in-Phase and Antiphase Coherences, J. Magn. Reson., Ser A 115 (2) (1995) 277–282.
[35] P. Villa-Valverde, I. Rodriguez, D. Padro, M. Benito, C.E. Garrido-Salmon, J. Ruiz-Cabello, A dual H-1/F-19 birdcage coil for small animals at 7T MRI, Magn. Reson. Mater. Phy. 32 (1) (2019) 79–87.
[36] P.A. Bottomley, T.H. Foster, R.E. Argersinger, L.M. Pfeifer, A Review of Normal Tissue Hydrogen Nmr Relaxation-Times and Relaxation Mechanisms from 1–100 Mhz - Dependence on Tissue-Type, Nmr Frequency, Temperature, Species, Excision, and Age, Med. Phys. 11 (4) (1984) 425–448.
[37] J.L. Evelhoch, J.J.H. Ackerman, Nmr T1-Measurements in Inhomogeneous-B1 with Surface Coils, J. Magn. Reson. 53 (1) (1983) 52–64.
[38] R. Colotti, J.A.M. Bastiaansen, A. Wilson, U. Flogel, C. Gonzales, J. Schwitter, M. Stuber, R.B. van Heeswijk, Characterization of perfluorocarbon relaxation times and their influence on the optimization of fluorine-19 MRI at 3 tesla, Magn. Reson. Med. 77 (6) (2017) 2263–2271.
[39] J. Ruiz-Cabello, P. Walczak, D.A. Kedziorek, V.P. Chacko, A.H. Schmieder, S.A. Wickline, G.M. Lanza, J.W.M. Bulte, In Vivo "Hot Spot" MR Imaging of Neural Stem Cells Using Fluorinated Nanoparticles, Magnet. Reson. Med. 60 (6) (2008) 1506–1511.
[40] S.H. Shin, D.K. Kadayakkara, J.W.M. Bulte, Hot spot 19F MR imaging of inflammation predicts colitis-associated cancer, Cancer Res. 75 (2015).
[41] P. Bouvain, S. Temme, U. Flogel, Hot spot F-19 magnetic resonance imaging of inflammation, Wires Nanomed. Nanobi. 12 (6) (2020).
[42] D.I. Hoult, Fast Recovery, High Sensitivity Nmr Probe and Pre-Amplifier for Low-Frequencies, Rev. Sci. Instrum. 50 (2) (1979) 193–200.
[43] D.I. Hoult, G. Kolansky, D. Kripiakevich, A 'hi-fi' Cartesian feedback spectrometer for precise quantitation and superior performance, J. Magn. Reson. 171 (1) (2004) 57–63.
[44] M. Sarracanie, C.D. LaPierre, N. Salameh, D.E.J. Waddington, T. Witzel, M.S. Rosen, Low-Cost High-Performance MRI, Sci Rep-Uk (2015;5.).
[45] K. Akazawa, F. Sugihara, T. Nakamura, H. Matsushita, H. Mukai, R. Akimoto, M. Minoshima, S. Mizukami, K. Kikuchi, Perfluorocarbon-Based F-19 MRI Nanoprobes for In Vivo Multicolor Imaging, Angew. Chem. Int. Ed. 57 (51) (2018) 16742–16747.

[46] J. Keupp, J. Rahmer, I. Grasslin, P.C. Mazurkewitz, T. Schaeffter, G.M. Lanza, S.A. Wickline, S.D. Caruthers, Simultaneous dual-nuclei imaging for motion corrected detection and quantification of 19F imaging agents, Magn. Reson. Med. 66 (4) (2011) 1116–1122.
[47] M. Meyerspeer, A.W. Magill, A. Kuehne, R. Gruetter, E. Moser, A.I. Schmid, Simultaneous and Interleaved Acquisition of NMR Signals from Different Nuclei with a Clinical MRI Scanner, Magnet. Reson. Med. 76 (5) (2016) 1636–1641.
[48] P.W. de Bruin, P. Koken, M.J. Versluis, S.A. Aussenhofer, I. Meulenbelt, P. Bornert, A.G. Webb, Time-efficient interleaved human Na-23 and H-1 data acquisition at 7 T, NMR Biomed. 28 (10) (2015) 1228–1235.